ACS OMEGA

http://pubs.acs.org/journal/acsodf

Article

Self-Assembled Interwoven Nanohierarchitectures of $NaNbO_3$ and $NaNb_{1-x}Ta_xO_3$ ($0.05 \leq x \leq 0.20$): Synthesis, Structural Characterization, Photocatalytic Applications, and Dielectric Properties

Umar Farooq, Jahangeer Ahmed, Saad M. Alshehri, Yuanbing Mao, and Tokeer Ahmad*

Cite This: *ACS Omega* 2022, 7, 16952−16967

Read Online

ACCESS | Metrics & More | Article Recommendations | Supporting Information

ABSTRACT: Dependence on fossil fuels for energy purposes leads to the global energy crises due to the nonrenewable nature and high CO_2 production for environmental pollution. Therefore, new ways of nanocatalysis for environmental remediation and sustainable energy resources are being explored. Herein, we report a facile surfactant free, low temperature, and environmentally benign hydrothermal route for development of pure and (5, 10, 15, and 20 mol %) Ta-doped horizontally and vertically interwoven $NaNbO_3$ nanohierarchitecture photocatalysts. To the best of our knowledge, such a type of hierarchical structure of $NaNbO_3$ has never been reported before, and changes in the microstructure of these nanoarchitectures on Ta-doping has also been examined for the first time. As-synthesized nanostructures were characterized by different techniques including X-ray diffraction analysis, electron microscopic studies, X-ray photoelectron spectroscopic studies, etc. Ta-doping considerably affects the microstructure of the nanohierarchitectures of $NaNbO_3$, which was analyzed by FESEM analysis. The UV−visible diffused reflectance spectroscopy study shows considerable change in the band gap of as-synthesized nanostructures and was found to be ranging from 2.8 to 3.5 eV in pure and different mole % Ta-doped $NaNbO_3$. With an increase in dopant concentration, the surface area increases and was equal to 5.8, 6.8, 7.0, 9.2, and 9.7 m^2/g for pure and 5, 10, 15, and 20 mol % Ta-doped $NaNbO_3$, respectively. Photocatalytic activity toward the degradation of methylene blue dye and H_2 evolution reaction shows the highest activity (89% dye removal and 21.4 mmol g^{-1} catalyst H_2 evolution) for the 10 mol % $NaNbO_3$ nanostructure which was attributed to a change in the conduction band maximum of the material. At 100 °C and 500 kHz, the dielectric constants of pure and 5, 10, 15, and 20 mol % Ta-doped $NaNbO_3$ were found to be 111, 510, 491, 488, and 187, respectively. The current study provides the rational insight into the design of nanohierarchitectures and how microstructure affects different properties of the material upon doping.

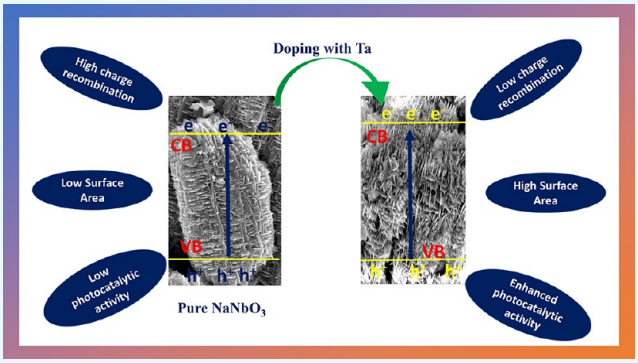

1. INTRODUCTION

The demand for environmentally benign materials for water remediation, energy generation, and storage applications has increased vastly due to the population explosion in last few decades.[1,2] Therefore, to meet the challenges due to exponential growing population, different new methods of environment remediation, green energy generation, and storage are being explored.[3−5] Among different techniques, photocatalytic remediation of wastewater and photocatalytic production of hydrogen from water splitting has gained prime importance due to being environment friendly and the renewable nature of water.[6,7] An important application of photocatalysis is the removal of hazardous organic pollutants from the water. To carry out the photocatalytic water splitting and degradation of organic pollutants from wastewater, different inorganic nano-photocatalysts like metal oxides ($NaNbO_3$, $NaTaO_3$, TiO_2, Cu_2O, Ag, $KNbO_3$, $La_{1-x}Sr_xCoO_3$, $Pr_2Sn_2O_7$, holmium oxide), metal tungstites, and molybdates have been used.[8−20] The use of diverse inorganic photocatalysts starts from the pioneering work carried out by Fujishima using TiO_2 as a photocatalyst for water splitting.[10] Among different explored photocatalysts, perovskite photocatalysts like $NaNbO_3$, $NaTaO_3$, $KNbO_3$, etc. have gained a lot of interest as an alternative to TiO_2 due to their environment friendly nature and comparable band gap to TiO_2.[8,9,11,12,21−23]

Received: December 23, 2021
Accepted: April 21, 2022
Published: May 9, 2022

https://doi.org/10.1021/acsomega.1c07250
ACS Omega 2022, 7, 16952−16967

With $NaNbO_3$ being a typical perovskite structure having a large pool of important properties like cost-effective, abundant, high crystallinity, environmentally friendly, and high chemical stability.[24,25] These properties make $NaNbO_3$ a fascinating material having great scientific, research, and technological interest. However, the large band gap associated with $NaNbO_3$ limits the prospect of utilizing it as an efficient photocatalyst. To have an excellent photocatalytic application of $NaNbO_3$, strenuous efforts are being made to improve the light absorption range and to limit the recombination rate of photogenerated charge carriers. In this context, different strategies like development of one-dimensional nanostructures (which show continuous electron transport thus retards the charge recombination), development of heterostructures between different photocatalysts[26] (which reduces the band gap and thus improves the absorption range of photocatalysts) and doping of the "Na" site or "Nb" site with different elements is being developed to improve the activity of $NaNbO_3$.[27,28] To control the band structure of the target photocatalysts, doping with foreign element is recognized as one of the potential strategies to improve the photocatalytic activity. The ionic charge balanced doping of Na site in $NaNbO_3$ perovskite has been mostly employed in improving the activity of the photocatalyst. Similarly, Jana et al., have used doping of rare earth metal to improve the photocatalytic activity of $NaTaO_3$. However, such a type of doping has little impact on the band structure.[29] In $NaNbO_3$, the conduction band is mainly constituted of the Nb^{5+} orbital and thus to change the electronic properties significantly doping of Nb site is more favorable. Jana et al. have studied the effect of doping of isovalent Nb^{5+} at the Ta^{5+} site on photocatalytic properties of $NaTaO_3$.[29] Also, Toresspardo et al. have studied the effect of substitution of Nb by isovalent Ta on electric and dielectric properties of $NaNb_{1-x}Ta_xO_3$.[30] To the best of our knowledge, $NaNb_{1-x}Ta_xO_3$ has not been investigated for its photocatalytic activity. However, the investigation of effect of doping of Nb by isovalent Ta on dielectric properties of $NaNb_{1-x}Ta_xO_3$ has been done previously, and the method used for synthesis of $NaNb_{1-x}Ta_xO_3$ include high temperature solid state reactions.[31] Also, to improve the properties the development of nanodimensional materials using different synthesis approaches like the solvothermal, polymeric precursor, hydrothermal, and reverse micellar methods and the use of different structure, morphology, and shape controlling agents have been employed.[32−38]

In addition to the development of new ways to generate energy, the demand for efficient energy storage materials is also increasing. More research and technological efforts are being made to develop high energy and power density materials which could further help in integration of miniaturized electronic devices. For this purpose, ceramic dielectric material has shown fascinating application due to their high chemical, mechanical, and thermal stabilities and high permittivity with high working temperature.

In this paper, low-temperature hydrothermal synthesis and structural characterization of pure $NaNbO_3$ and $NaNb_{1-x}Ta_xO_3$ were carried out. The photocatalytic applications of synthesized hierarchical interwoven nano $NaNb_{1-x}Ta_xO_3$ was screened by carrying out the degradation of organic pollutant and by carrying out H_2 evolution from the water splitting reaction. With varying the concentration of Ta doping, the interwoven nanohierarchitecture of $NaNb_{1-x}Ta_xO_3$ showed improved photocatalytic activity compared to pure $NaNbO_3$. In addition to photocatalytic application, the effect of doping of isovalent Ta at the Nb site on dielectric properties of $NaNbO_3$ was also investigated. From the investigation, it was observed that doping of Nb by isovalent Ta improves both photocatalytic activity and dielectric properties of $NaNbO_3$ nanoparticles. The changes in both photocatalytic activity and dielectric properties of Ta doped $NaNbO_3$ were correlated with the possible changes in the band structure and microstructure taken place due to doping of Ta.

2. EXPERIMENTAL SECTION

2.1. Materials. All the chemicals used in the synthesis process were of analytical grade. To synthesize pure $NaNbO_3$ and $NaNb_{1-x}Ta_xO_3$, NaOH (Merck, 97%) was used as a source of Na. Nb_2O_5 (Alfa Aesar, 99%) was used as a precursor for Nb, and Ta_2O_5 (Alfa Aesar) was used as the Ta source. To check the photocatalytic removal of organic pollutants, methylene blue dye (MB) (Merck) was used as a model pollutant. Other chemicals used include silver nitrate (Merck, 99.5%), benzoquinone (Merck, 97%), ammonium oxalate (Merck, 30%), and isopropanol (RANKEM, 99%). All the chemicals were used as received without further purification.

2.2. Synthesis of Sodium Niobate Nanohierarchitecture. Sodium niobate nanoparticles with hierarchitectured morphology were first time synthesized by using a simple low-temperature hydrothermal route. The hydrothermal route employed for the synthesis of pure $NaNbO_3$ nanoparticles is reported somewhere else.[25] In a typical synthesis process, 0.025 mol of Nb_2O_5 was added in 10 M NaOH solution. The solution was stirred at room temperature for 4 h. After that, the solution was transferred to a 75 mL Teflon lined autoclave and was heated at 180 °C for 4 h. The solution could cool naturally and was centrifuged and then washed several times, first with distilled water and then with ethanol.

2.3. Synthesis of Ta Doped Sodium Niobate Nanohierarchitecture. $NaNbO_3$ doped with different concentrations of Ta was synthesized by a similar hydrothermal route except the addition of Ta_2O_5 as a precursor for Ta. In a typical synthesis process, 0.025 mol of Nb_2O_5 was added to 10 M solution of NaOH followed by addition of 5, 10, 15, and 20 mol % of Ta_2O_5 in the reaction mixture. The whole reaction mixture was stirred for 4 h and transferred to a 75 mL Teflon lined autoclave. The reaction mixture was heated at 180 °C for 4 h and then cooled to room temperature. To get the final product, the reaction mixture was centrifuged at 7000 rpm and was washed with distilled water and ethanol several times. The final product was dried in a vacuum oven at 60 °C and was used for further analysis. All the synthesized samples were coded as (NN) for pure $NaNbO_3$ and NN1, NN2, NN3, and NN4 for 5%, 10%, 15% and 20% Ta doped $NaNbO_3$, respectively.

2.4. Characterization. Powder X-ray diffraction analysis (XRD) was carried out by employing a Rigaku diffractometer using Cu Kα radiation having a wavelength equal to 1.5406 Å. All the samples were scanned with a scan rate and step size equal to 5°/min and 0.02°, respectively. X-ray diffraction analysis was carried out with 2θ ranging from 10 to 70°. Fourier transformation infrared spectroscopic (FTIR) analysis was carried out by using pellets of as synthesized samples in the presence of KBr. FTIR analysis was carried out using a PerkinElmer FT-IR spectrophotometer model IR affinity1. Transmission electron microscope (TEM) analysis was carried out by using the samples dispersed in ethanol and mounted on a carbon coated copper grid. The grids for TEM analysis were prepared by carrying out the drop casting of the sample on the

https://doi.org/10.1021/acsomega.1c07250
ACS Omega 2022, 7, 16952−16967

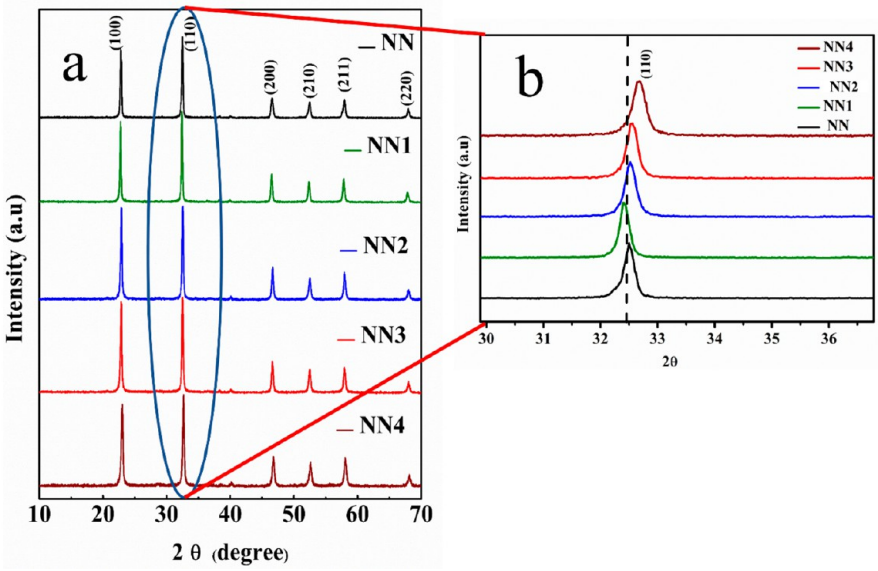

Figure 1. (a) XRD patterns of the as-synthesized NN, NN1, NN2, NN3, and NN4 nanostructures and (b) zoomed in XRD pattern showing shifting of peaks with Ta doping.

copper grid. TEM analysis was done using a TELOS instrument with an accelerating voltage of 200 kV. For field emission scanning electron microscopy (FESEM), samples were mounted in the form of powder on the grid with gold coating. FESEM analysis was carried out using FEI NOVA NanoSEM 450 having an accelerating voltage of 20 kV. In addition to FESEM, EDAX and elemental mapping of the samples was carried out using FEI NOVA NanoSEM 450. The binding energy and oxidation state analysis of the samples was carried out by using X-ray photoelectron spectroscopy (XPS). XPS analysis was carried out in survey mode by carrying out surface charge neutralization. For XPS analysis operating a flood gun having 30 eV pass energy, a 0.01 eV step size was used. All the peaks in the XPS spectra were calibrated with respect to C 1s having a peak position at 284.8 eV. XPS measurements were carried out using Thermoscientific XPS having Al Kα radiation, with $h\upsilon$ = 1486.6 eV. The band gap was determined by using diffused reflectance UV−vis spectroscopy (DRS). Reflectance analysis of the samples was carried out using a PerkinElmer Lambda365 UV−vis spectrophotometer with $BaSO_4$ as a reference sample in the range of 200−800 nm. By employing reflectance data, a band gap was calculated using the Kubelka−Munk equation. Surface area analysis was carried out by using the Brunauer−Emmett−Teller (BET) surface area analysis technique. For surface area analysis, a Nova 2000e (Quantachrome Instruments Limited, USA) was used. All the measurements were carried out in the presence of liquid nitrogen having a bath temperature of 77 K. Before carrying out the analysis, all the samples were degassed under vacuum conditions at 150 °C for 12 h to remove the unwanted adsorbed gases on the samples. The weight of the samples was measured before and after degassing to calculate the actual amount of sample having no adsorbed gases on their surfaces. Photoluminescence (PL) analysis of the synthesized samples was carried out by using an F-7000 Hitachi fluorescence spectrophotometer with an excitation wavelength ranging from 400 to 500 nm.

2.5. Photocatalytic Studies. Degradation of methylene blue was carried out in the presence of sunlight to elucidate the photocatalytic activity of as-prepared nanoparticles. To carry out the analysis, a stock solution of MB dye having a concentration equal to 1×10^{-5} M was prepared in aqueous medium. A total of 20 mg of nanoparticles was dispersed in 50 mL of the dye solution and was kept in the dark for 1 h to ensure adsorption−desorption equilibrium between the dye and the nanocatalysts. The dye-catalyst suspension was then exposed to sunlight irradiation to initiate the photocatalytic degradation reaction. After every 10 min, adequate aliquots were taken and centrifuged to remove the suspended catalyst particulates for spectral analysis. Similar experiments were carried out either in the dark or without catalysts to confirm the degradation process is solely photocatalytic driven. The efficiency of the catalyst for photodegradation process was monitored by a change in intensity of the characteristic absorption peak of MB at ∼664 nm using a PerkinElmer Lambda365 UV−vis spectrophotometer. The percentage removal of the dye was computed by using eq 1.

$$\text{Percent Removal}\,(\%) = C_i - \frac{C_f}{C_i} \times 100 \quad (1)$$

where C_i is the initial concentration of MB dye after adsorption−desorption equilibrium before irradiation and C_f is the concentration of dye after time interval t (in minutes). In addition to UV−visible spectra, liquid chromatography-mass spectrometry (LC-MS) of the dye solution was carried out to attest whether the dye has been degraded or not. Mass spectral studies were carried out by using an API2000 Applied Biosystems LC/MS/MS/MS instrument.

2.6. Photocatalytic Water Splitting Measurements. The photocatalytic activities for hydrogen generation were also studied for all synthesized samples in an external irradiation cell with a light source of a 200 W Hg (Xe) lamp (New Port, Mercury−Xenon, 200 W model 66906-200HXF-R15 ozone-free) at an intensity of 190 W without a cutoff filter under full arc irradiation. For the photocatalytic H_2 evolution experiments, a 100 mL cylindrical quartz cell with its flat surfaces being exposed to the light source was charged by 20 mg of the photocatalyst and 0.128 moles of Na_2S, 0.079 moles of Na_2SO_3 as the sacrificial agents were dispersed uniformly in 50 mL of double distilled water. The cell containing the solution was closed with

https://doi.org/10.1021/acsomega.1c07250
ACS Omega 2022, 7, 16952−16967

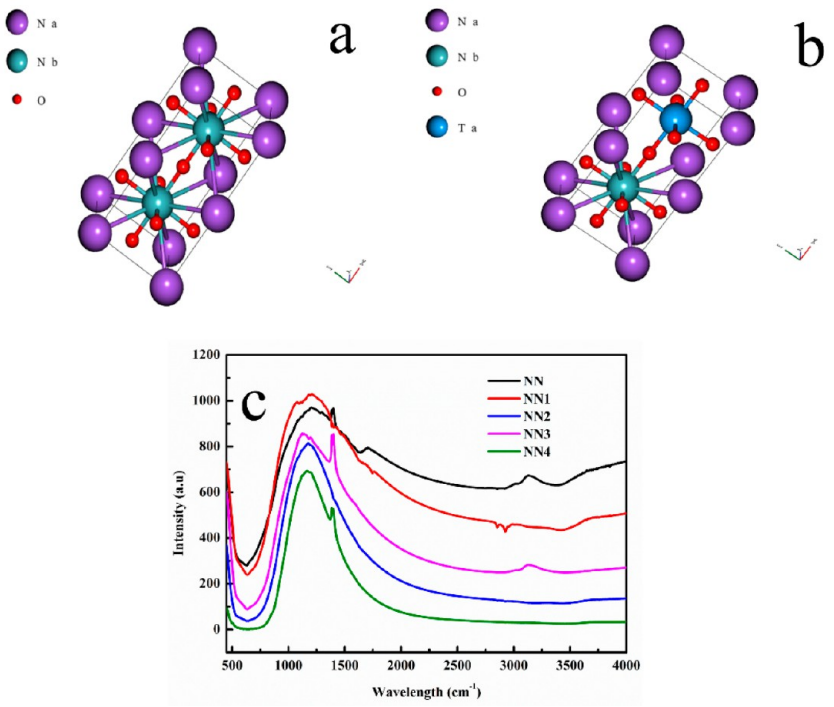

Figure 2. Crystal structure of (a) pure $NaNbO_3$ and (b) Ta-doped $NaNbO_3$ obtained by using Quantum espresso software and (c) FTIR spectra of as synthesized samples (NN, NN1−NN4).

an airtight rubber septum at the top and kept in an inert atmosphere by purging N_2 gas into the cell for half an hour prior to carrying out the measurements and to remove any impurities of the gases. After degassing, the solution mixture was placed under light on constant stirring and kept at a constant temperature of around (25 °C). The quantification of the amount of evolved H_2 gas was done by using gas chromatography (PerkinElmer, Clarus 590 GC) equipped with a TCD detector using N_2 as the carrier gas. The gaseous components were monitored by per hour sampling, and evolved H_2 was estimated with the reference hydrogen gas by comparing the GC plot.

2.7. Dielectric Measurements. Dielectric properties of the as-prepared samples were measured using 6505 P, Wayne Kerr Electronics, U.K. Dielectric properties of the samples were analyzed as a function of frequency and temperature ranging from 20 Hz to 1 MHz and 50−500 °C respectively. To study the dielectric properties of the synthesized samples, a parallel plate capacitor was developed by using sample disks having a 8 mm diameter and 0.8 mm thickness and coated with a silver conducting surface which acts as an electrode. For the preparation of pellets, poly(vinyl alcohol) (PVA) was used as a binder. All the synthesized samples were mixed with 5% PVA in a mortar and pestle, and pellets were formed by applying pressure equal to 5 tons using a technosearch KBr press model M-5. All the pellets were annealed at 800 °C before dielectric measurements were carried out.

3. RESULTS AND DISCUSSION

3.1. X-ray Diffraction (XRD) Studies. The phase composition, phase purity, crystal structure, and crystallinity of pure $NaNbO_3$ and $NaNb_{1-x}Ta_xO_3$ having different compositions of Ta (5−20 mol %) was determined by XRD analysis as shown in Figure 1a. From the XRD patterns, it was observed that pure monophasic $NaNbO_3$ having an orthorhombic crystal structure was synthesized using the hydrothermal route. All the reflection peaks observed in the XRD were matched with the JCPDS card no. 89-5173. The resultant Ta doped $NaNbO_3$ samples have quite identical isostructural orthorhombic crystal structures. Peaks at 2θ values of 22.89°, 32.77°, 46.85°, 52.61°, 58.06°, and 68.19° correspond to (100), (110), (200), (210), (211), and (220) crystal planes, respectively. With an increase in concentration of Ta in $NaNbO_3$, the peaks are little shifted toward higher 2θ values as shown in Figure 1b, and this apparent shifting in peaks was attributed to the small ionic radii of Ta (0.64 nm) as compared to Nb (0.72 nm) thus causing the lattice contraction in Ta-doped $NaNbO_3$ samples.[39] The XRD results obtained were employed to determine the crystallite size of the as-synthesized nanoparticles. To determine the crystallite size, Scherrer's equation was used, and the calculated crystallite sizes were equal to 23.1, 27.9, 24.9, 24.6, and 20.3 nm for NN, NN1, NN2, NN3, and NN4 samples, respectively. Using XRD results, the crystal parameters and crystal structure of as-synthesized nanoparticles were deduced by using Quantum espreso software. Using the XRD results along with the crystallography open database (COD) file for $NaNbO_3$, the crystal structure of the as synthesized $NaNbO_3$ was deduced. The obtained crystal structures are shown in Figure 2a,b for pure $NaNbO_3$ and Ta-doped $NaNbO_3$ nanostructures, respectively.

3.2. Fourier Transformation Infrared Spectroscopic (FTIR) Studies. FTIR studies were carried out to determine the formation of M−O bond using KBr as a carrier for as synthesized samples. Figure 2c represents the IR spectra (500−4000 cm^{-1}) of as synthesized samples. From the obtained results, the peak present between 500 and 650 cm^{-1} confirms the formation of a metal oxide (M−O) bond. In all the synthesized samples, the IR peak is present at 625 cm^{-1} and thus confirms the successful formation of Ta−O or Nb−O bonds, and no other prominent peaks were observed in any of the synthesized samples.

https://doi.org/10.1021/acsomega.1c07250
ACS Omega 2022, 7, 16952−16967

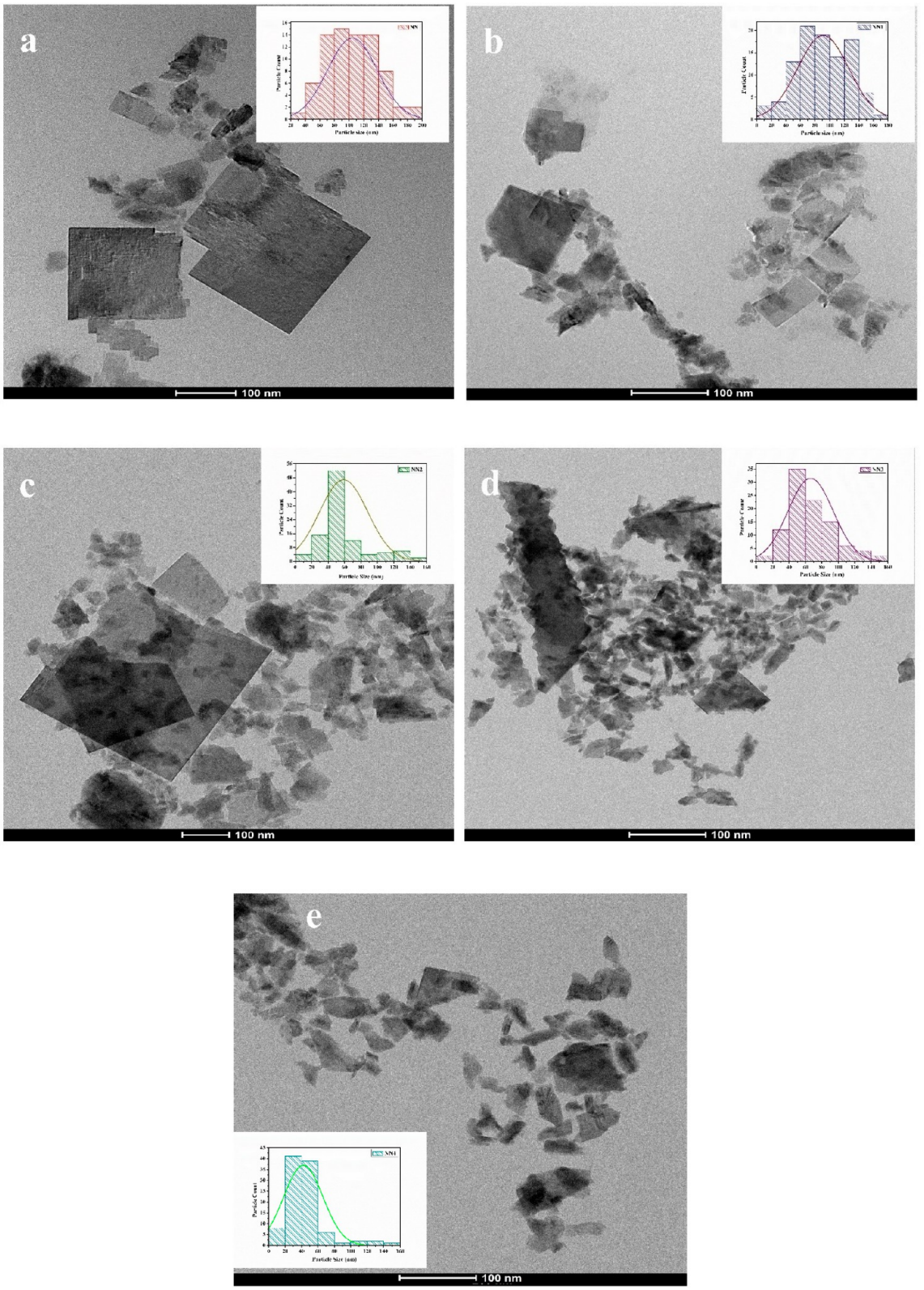

Figure 3. TEM micrographs and particle size distribution histograms (inset) of (a) NN, (b) NN1, (c) NN2, (d) NN3, and (e) NN4 nanostructures.

3.3. Transmission Electron Microscopic (TEM) Studies.

Figure 3 represents the TEM micrographs of the as-prepared samples. From TEM analysis, it was observed that typical single layered pure $NaNbO_3$ nanoflakes were synthesized successfully as evident in Figure 3a. With the addition of Ta as a dopant, the formation of the layered structure is restricted as observed in Figure 3b−e. From TEM analysis, it was observed that above 10 mol % Ta doping, the small flake shaped particles start to appear

https://doi.org/10.1021/acsomega.1c07250
ACS Omega 2022, 7, 16952−16967

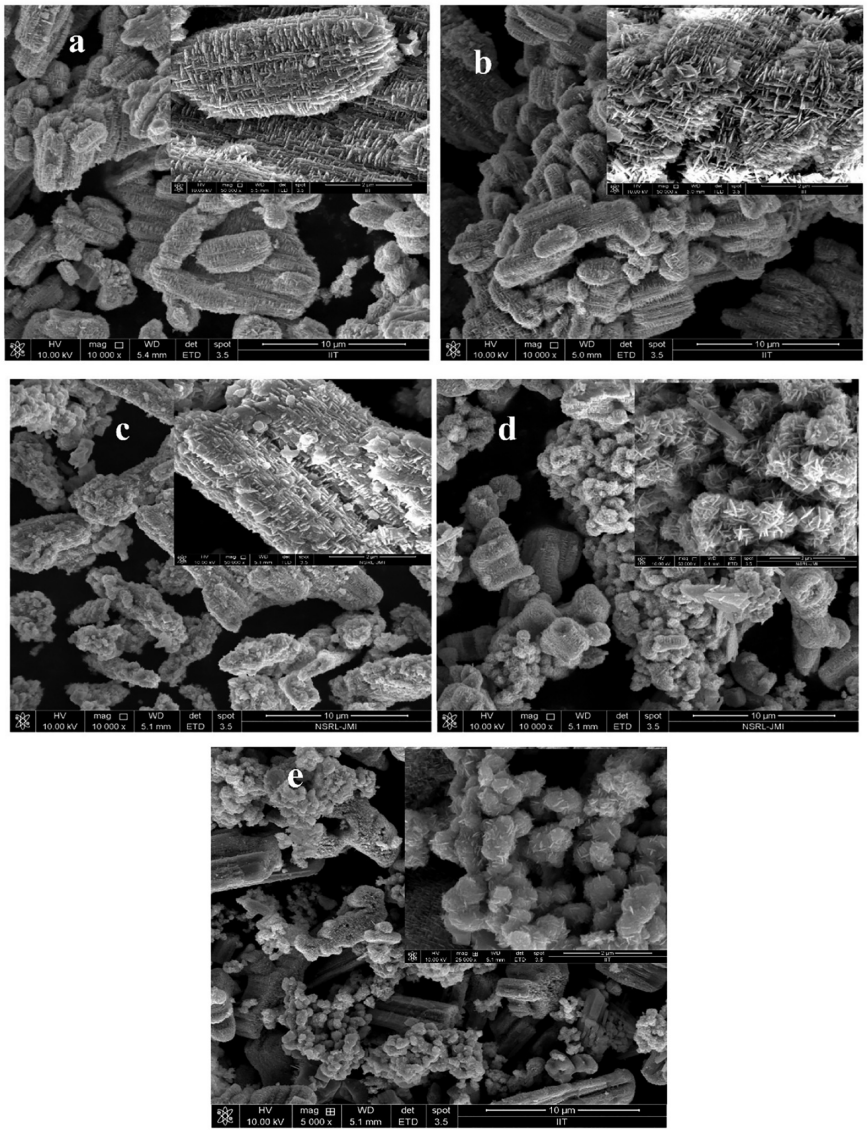

Figure 4. FESEM micrographs of (a) NN, (b) NN1, (c) NN2, (d) NN3, and (e) NN4 nanostructures.

as shown in Figure 3d,e. From the TEM micrographs of the as-synthesized samples, the average particle size distribution was calculated and the obtained histogram is represented in the inset of Figure 3a−e. The average particle sizes for the samples NN, NN1, NN2, NN3, and NN4 were found to be 100, 90, 60, 70, and 40 nm, respectively. To the best of our knowledge, no such flake-like layered nanoparticles of pure $NaNbO_3$ and Ta-doped $NaNbO_3$ have been reported previously.

3.4. Field Emission Scanning Electron Microscopic (FESEM) Studies. The FESEM technique was used to investigate the microstructure and micromorphology of as-prepared pure $NaNbO_3$ and Ta-doped $NaNbO_3$ samples. FESEM micrographs of all the samples are shown in Figure 4. It is observed that as-prepared pure $NaNbO_3$ shows large building blocks with hierarchical arrangement of intercrossed horizontal and vertical nanoflakes (Figure 4a). Similarly, in 5% Ta doped $NaNbO_3$, the interwoven nanoflakes are present but the hierarchy is slightly disturbed. With a further increase in concentration of Ta to 10 mol %, intercrossed nanoflakes decrease and little particle formation starts to appear. A further increase in the concentration to 15 and 20 mol %, the needle shaped particles with flowerlike structures are formed. The magnified FESEM micrographs of as-synthesized nanostructures are shown in Figure S1a−e. The detailed observation of the single building blocks showed that these blocks are composed of several small flakes. These small flakes are interconnected horizontally and vertically, thus forming a hierarchical structure. It was also observed that the surface of small flakes was not smooth, which was attributed to Ostwald ripening/coarsening.[40] Figure S1f−j further demonstrate that the nanoflakes were composed of small nanoparticles.

To determine the elemental composition of the as-synthesized pure and Ta-doped $NaNbO_3$ nanoflakes, EDAX analysis was carried out. From the EDAX study, it was observed that peaks in the spectra correspond to Na, Nb, and O with no impure peak present in the $NaNbO_3$ sample as shown in Figure S2a. EDAX of the $NaNbO_3$ samples doped with Ta show the presence of Ta in the spectra (Figure S2b−e). Also, from the EDAX of the samples, it was observed that with increasing the concentration of Ta, the atomic weight percent of Nb decreases which is due to the fact that Ta is doped at Nb sites of the samples. The atomic weight percentage of different constituent

https://doi.org/10.1021/acsomega.1c07250
ACS Omega 2022, 7, 16952−16967

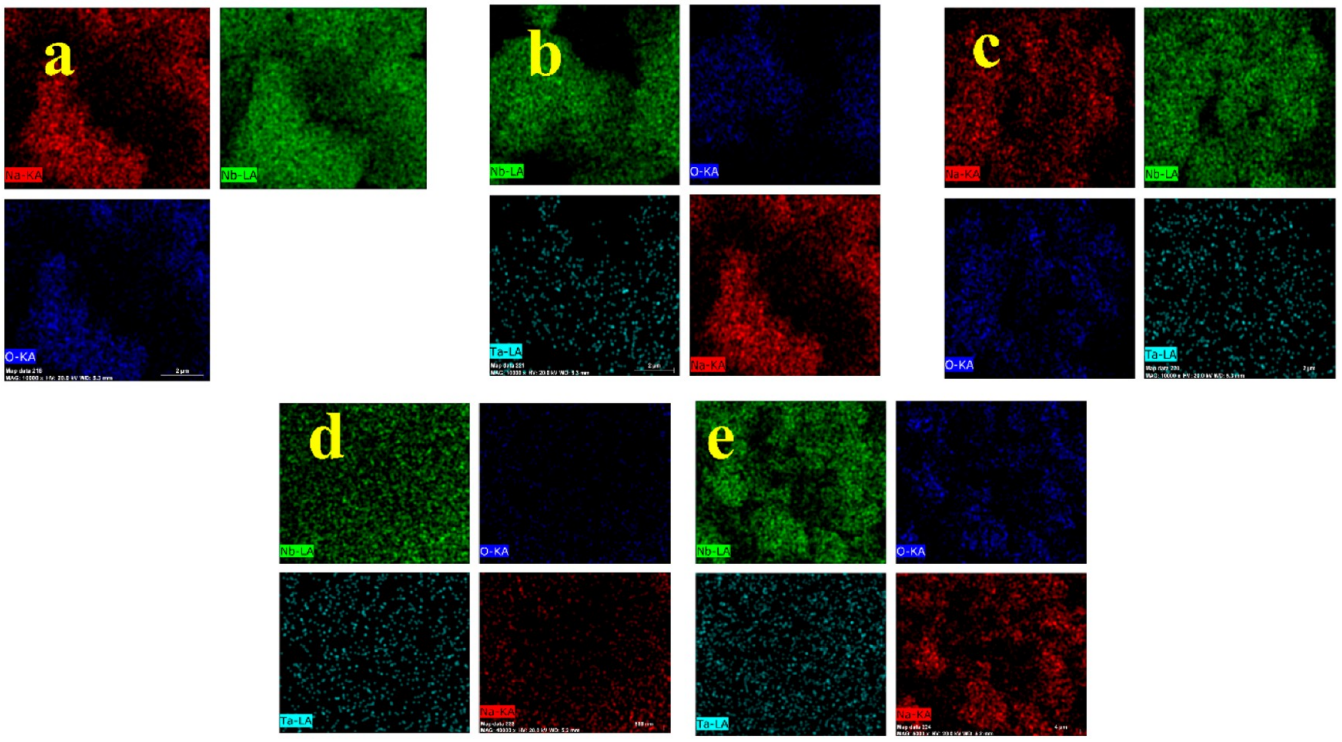

Figure 5. Elemental mapping of (a) NN, (b) NN1, (c) NN2, (d) NN3, and (e) NN4 nanostructures.

elements of the as synthesized nanostructures is given in Table S1. In addition to EDAX analysis, elemental mapping of the as-prepared samples was carried out. Figure 5a−e shows the elemental mapping of pristine $NaNbO_3$ (NN) and Ta-doped $NaNbO_3$ (NN1−NN4) samples. From element mapping of all the samples, it was seen that Na, Nb, and O are distributed uniformly in pristine $NaNbO_3$ sample, whereas, in the samples doped with Ta, coexistence of Ta along with other elements was observed. It was also observed that the density of Ta distribution in all Ta-doped samples increases with an increase in concentration of Ta.

3.5. X-ray Photoelectron Spectroscopy (XPS) Study. Oxidation state and the surface chemical composition of the synthesized photocatalyst samples were elucidated by employing the XPS technique. The binding energies of all the samples were calibrated with respect to C 1s having a binding energy centered at 285.8 eV. Figure 6a represents the survey spectra of pure $NaNbO_3$ and Ta doped (with different mole %) $NaNbO_3$ nanoparticles. From the survey scan of pure $NaNbO_3$, the peaks corresponding to Nb, Na, and O were present. While as in addition to the peaks corresponding to Na, Nb, and O, a peak corresponding to Ta was also present in the samples doped with 10, 15, and 20 mol % Ta. From the XPS analysis, it was observed that no peak corresponding to Ta in the sample with 5 mol % of Ta doping was observed. This was due to a low concentration of Ta present on the surface of the sample. High-resolution XPS of all the samples was carried out as shown in Figure 6. Figure 6b represents the high-resolution XPS spectra of Na with peak centered at 1071 eV, which corresponds to Na 1s.[8] The peak present at 1071 eV shows that Na is present in +1 oxidation in all the synthesized samples. Figure 6c represents the high-resolution XPS spectra of O 1s, which is centered at a binding energy equal to 529 eV confirming the −2 oxidation state of O.[41] The peak corresponding to O 1s originates due to −Nb−O in pure $NaNbO_3$ or due to −Ta−O present in Ta-doped $NaNbO_3$ samples. Figure 6d shows the high-resolution XPS spectra of Nb element present in the synthesized photocatalysts. The peak corresponding to Nb 3d was deconvoluted into two peaks centered at 206.3 and 209.5 eV, which corresponds to Nb $3d_{5/2}$ and Nb $3d_{3/2}$, respectively.[42] The difference between the two deconvoluted peaks corresponding to Nb was found to be 3 eV, which evidenced that Nb is present in the +5 oxidation state in all the synthesized samples.[43] Figure 6e corresponds to the high-resolution XPS spectra of Ta. Ta present in the prepared samples shows a doublet of peaks of spin orbit coupling (7/2 and 5/2). The peaks centered at 25.6 and 27.7 eV correspond to the Ta $4f_{7/2}$ and Ta $4f_{5/2}$, respectively. The binding energy corresponding to 7/2 (25.6 eV) is consistent with previously reported data and confirms the +5 oxidation state of Ta cations.[44] From the XPS results, it was confirmed that Ta was successfully incorporated at Nb sites upon doping in $NaNbO_3$ photocatalysts.

3.6. Diffused UV−Visible Reflectance Spectroscopy (DRS) Study. UV−vis DRS spectra of the synthesized samples are shown in Figure S3. Figure S3a shows the reflectance spectra of the as-synthesized samples. The obtained reflectance data was used to calculate the band gap of the materials using the Kubelka−Munk equation. Reflectance was converted to absorbance of the samples using eq 2.

$$F(R) = a/s = (1 - R)^2/2R \quad (2)$$

In eq 2, $F(R_\infty)$ represents the Kubelka−Munk function and is equal to the diffused reflectance of the infinite thick sample, the terms F, α, s, and R represent the Kubelka−Munk function, absorption coefficient, scattering factor, and reflectance of the material, respectively. Figure S3b represents the plot of band gap energy versus $(F(R_\infty)h\nu)^{1/n}$. From the DRS study, it was observed that pure $NaNbO_3$ shows a band gap equal to 2.89 eV,

https://doi.org/10.1021/acsomega.1c07250
ACS Omega 2022, 7, 16952−16967

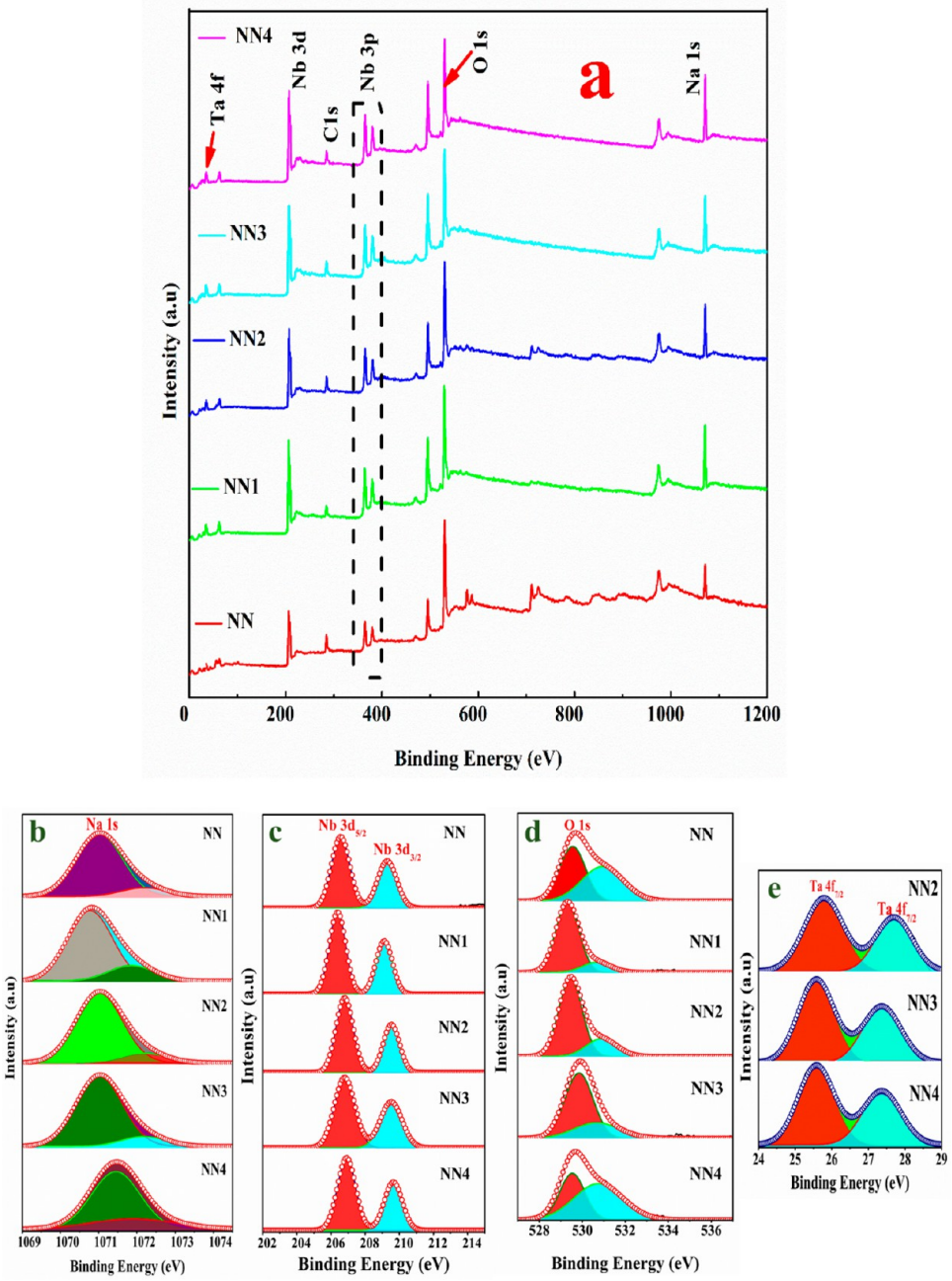

Figure 6. (a) Full range XPS spectra of the as-synthesized photocatalysts (NN−NN4). High-resolution XPS spectra of (b) Na 1s, (c) O 1s, (d) Nb 3d, and (e) Ta 4f present in the NN, NN1, NN2, NN3, and NN4 nanostructures.

whereas the photocatalysts doped with 5, 10, 15, and 20 mol % Ta have band gaps equal to 2.92, 3.0, 3.18, and 3.2 eV, respectively. The band gap calculated in this report for pure $NaNbO_3$ is in accordance to the previously reported results.[45] From the calculated bandgap, it is observed that the band gap of Ta-doped $NaNbO_3$ photocatalysts is more than pure $NaNbO_3$. The increase in the band gap is due to substitution of Ta^{5+} at Nb^{5+} sites in the pristine $NaNbO_3$ photocatalyst. In most of the metal oxides, the O 2p and d orbital of the transition metal constitute the valence and conduction bands, respectively. Thus, the top of the valence band of each prepared sample comprises the O 2p orbital. By substitution of Ta at Nb sites, the conduction potential of Ta-doped $NaNbO_3$ becomes more negative, thus resulting in an increase in the band gap of the as-synthesized Ta-doped nanostructures. This more negative conduction potential is considered as beneficial for driving and separation of photogenerated charge carriers, which could be highly useful for improved photocatalytic activity of the synthesized nanoparticles. However, the large bandgap of a material decreases the absorption range of a photocatalytic material which could reduce the activity of a material as a photocatalyst.

3.7. Brunauer−Emmett−Teller (BET) Surface Area Analysis. Surface area of the sample plays vital role in the catalytic activity of the materials. BET surface area analysis was used to determine the surface area of the synthesized samples. Figure 7a shows the BET N_2 adsorption−desorption isotherm of as prepared photocatalysts. From the BET surface area measurements, it was observed that all the samples show type IV adsorption isotherms with a H3 hysteresis loop which

https://doi.org/10.1021/acsomega.1c07250
ACS Omega 2022, 7, 16952−16967

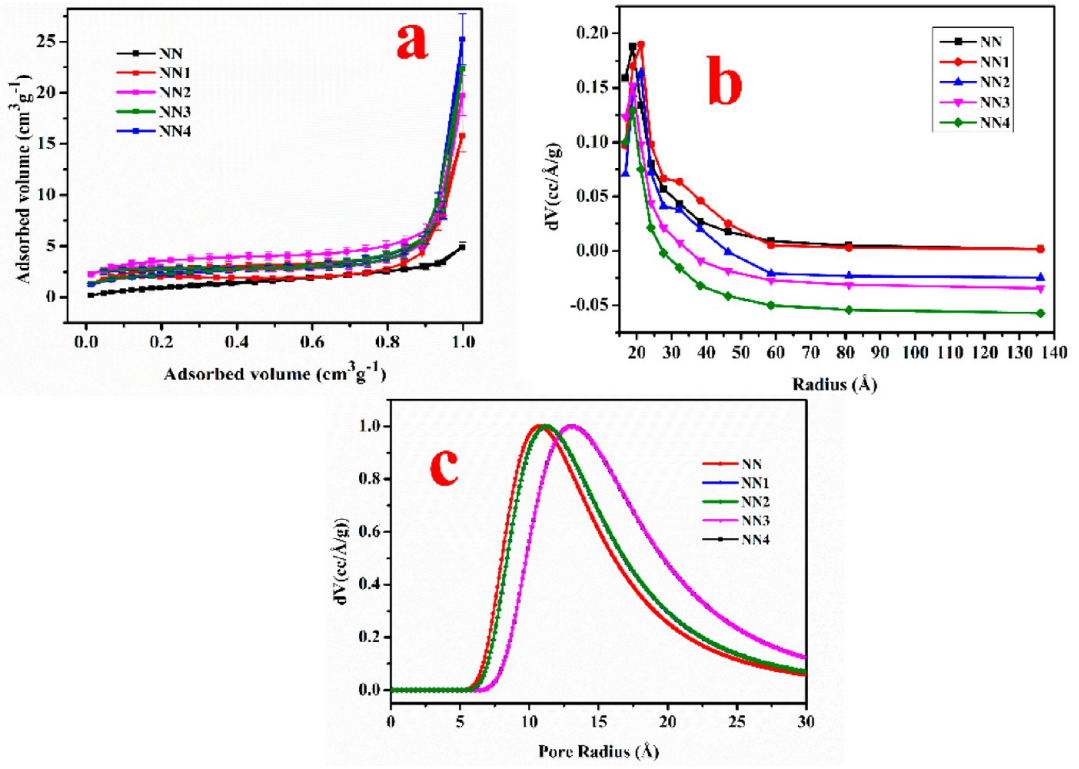

Figure 7. (a) N_2 adsorption desorption isotherms, (b) BJH plots, and (c) DA plots of as-prepared nanostructures.

confirms the as prepared nanoparticles are having a well-defined mesoporous structure.[46] This type of isotherm indicates that multilayer adsorption is taking place followed by condensation. The isotherm possesses a hysteresis loop which is formed because of condensation process taking place on mesoporous solids.[47] Using desorption points, the pore size distribution of as-prepared samples was evaluated from the Barrett–Joyner–Halenda (BJH) plot as shown in Figure 7b. From the BJH plot, it was observed that all the samples show monomodal pore distribution centered between 15 and 20 Å. The average pore size of all the samples was deduced from adsorption desorption points of the isotherm by using Dubinin–Astakhov (DA) analysis. Figure 7c represents the DA plot of synthesized $NaNbO_3$ and Ta doped $NaNbO_3$ nanoparticles. The specific surface area, DA average pore size, and BJH pore radius of the samples calculated from BET analysis is given in Table 1. From

Table 1. BET Surface Area, DA Pore Size, and BJH Pore Size Distribution of As-Synthesized Nanohierarchitectures

sample	BET surface area (m^2/g)	DA average pore size (Å)	BJH pore size distribution (Å)
NN	5.8	11.6	18.7
NN-1	6.8	13.3	18.8
NN-2	7	11.3	18.7
NN-3	9.2	11.1	18.8
NN-4	9.7	11.7	18.8

the BET studies, it was observed that using the hydrothermal route, nanoparticles with enhanced surface area were obtained compared to the samples prepared by the conventional solid state route.[44] Also, it was observed that with an increase in the amount of Ta, the surface area increases which was attributed to formation of small particles as observed in TEM and FESEM analysis.

3.8. Photocatalytic Studies. *3.8.1. Photocatalytic Dye Degradation Studies.* To check the photocatalytic activity of as-prepared nanoparticles, methylene blue (MB) was used as a model pollutant. A 1×10^{-5} M stock solution of MB was prepared followed by addition of 20 mg of as-prepared photocatalysts. The dye solution along with the photocatalyst nanoparticles were kept under dark condition for 1 h to attain adsorption desorption equilibrium. From the adsorption study, it was observed that the negligible amount of dye has been adsorbed on the catalyst surface. Also, the dye solution without photocatalyst was exposed to sunlight to check the photolysis of MB dye. After adsorption–desorption equilibrium, the dye solution was exposed to solar radiations. After every 10 min, 3 mL of dye solution was extracted to check the change in the absorption maxima of the MB dye in the presence of solar radiation and photocatalyst. The process of photocatalysis was carried out for 80 min. Figure S4a–e represents the UV–visible absorption spectra of MB dye in the presence of as-synthesized photocatalysts and light. From Figure S4a–e, it was observed that with an increase in exposure time, the intensity of absorption maxima of MB dye decreases continuously, confirming the degradation of MB dye with time in the presence of sunlight and as-synthesized photocatalysts. From UV–vis spectra it was also observed that with an increase in Ta doping up to 10 mol %, the photocatalytic activity of $NaNbO_3$ increases, and with a further increase in concentration of dopant the photocatalytic activity decreases. Using UV–visible absorption spectra, percentage removal of MB dye was calculated as represented in Figure 8a. From the obtained results, a maximum decrease in the concentration of MB dye was observed in 10 mol % Ta doped $NaNbO_3$ photocatalyst. From Figure 8a, maximum degradation of 89% was observed in 10 mol % Ta doped

https://doi.org/10.1021/acsomega.1c07250
ACS Omega 2022, 7, 16952–16967

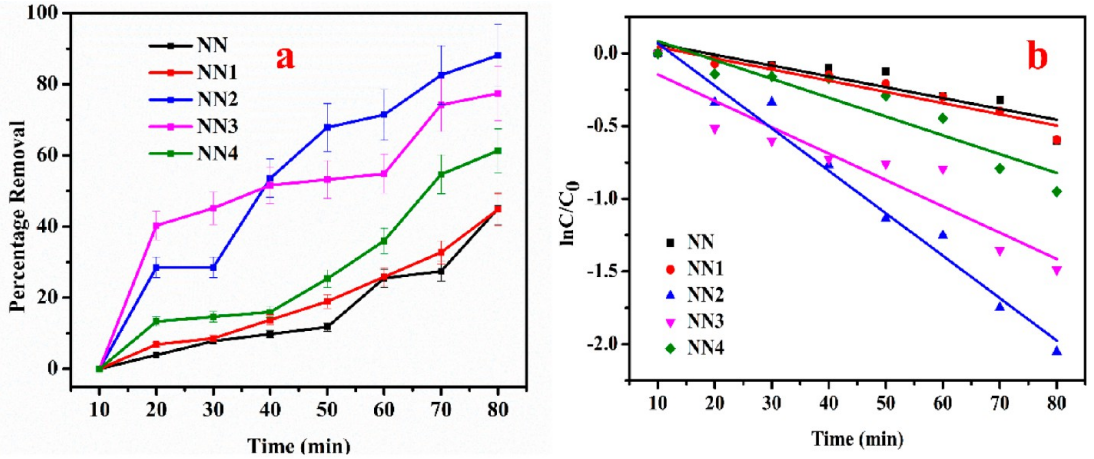

Figure 8. (a) Percentage removal efficiency and (b) kinetic plots of the photocatalytic degradation reaction using the as-synthesized pure and Ta-doped $NaNbO_3$ photocatalysts.

$NaNbO_3$. The percentage removal of MB dye using different photocatalysts is tabulated in Table 2. To determine the kinetics of the photocatalytic degradation reaction of MB dye using as-synthesized nanoparticles, different models were used. From the kinetic study, it was observed that all the synthesized photocatalysts obey the Langmuir–Hinshelwood mechanism as shown in Figure 8b. The kinetics of the photocatalysts was determined by using eq 3.

Table 2. Percentage Removal of MB Dye and Rate Constant of Photocatalytic Reactions Carried out by the Synthesized Nanocatalysts

sample	percentage removal	rate constant	R^2
NN	44.90	0.12	0.97
NN1	44.90	0.13	0.99
NN2	89	0.36	0.98
NN3	74.84	0.21	0.97
NN4	60.96	0.16	0.96

$$\text{Ln } C/C_0 = kKt = Rt \quad (3)$$

where C and C_0 represents concentration after time t and initial concentration at $t = 0$, respectively, and R is the rate constant of the photocatalytic reaction. From the kinetic study, it was observed that degradation process carried out by as-synthesized photocatalysts follow pseudo first order kinetics, which was confirmed by the straight line obtained from the semi-logarithmic plot of concentration versus irradiation time. The rate constant of the degradation process was determined by using linear fitting of the curves. Table 2 shows the rate constant and R^2 values of the photocatalytic degradation process of the MB dye in the presence of pure and Ta-doped $NaNbO_3$ photocatalysts.

In addition to UV–visible spectral studies, the degradation of MB dye was confirmed by using LC-MS. The samples with least intensity (obtained after 80 min) in the UV–vis spectra were used to carry out the LC-MS analysis. LC-MS spectra of MB dye after carrying out photocatalytic degradation using as-synthesized photocatalysts are shown in Figure S5a–e. The possible chemical formulas and structure of degradation fragments obtained from LC-MS spectra were deduced using the Chemdraw structural tool and are shown in Figure S6a–e. The role of different active species ($OH^{\bullet}$, $O_2^{\bullet-}$, e^-, H^+) generated during the photocatalytic process was elucidated by carrying out the quenching process using different scavengers as discussed in the Supporting Information of the manuscript.

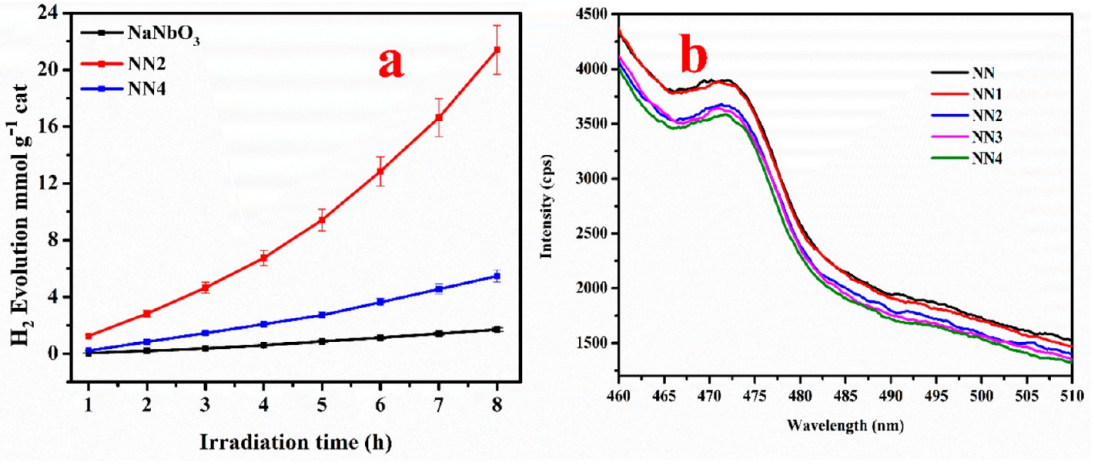

Figure 9. (a) Photocatalytic hydrogen evolution of pure and Ta-doped $NaNbO_3$ photocatalysts with irradiation time using Na_2S and Na_2SO_3 as sacrificial agents, and (b) PL spectra of pure and Ta-doped $NaNbO_3$ nanoparticles.

https://doi.org/10.1021/acsomega.1c07250
ACS Omega 2022, 7, 16952–16967

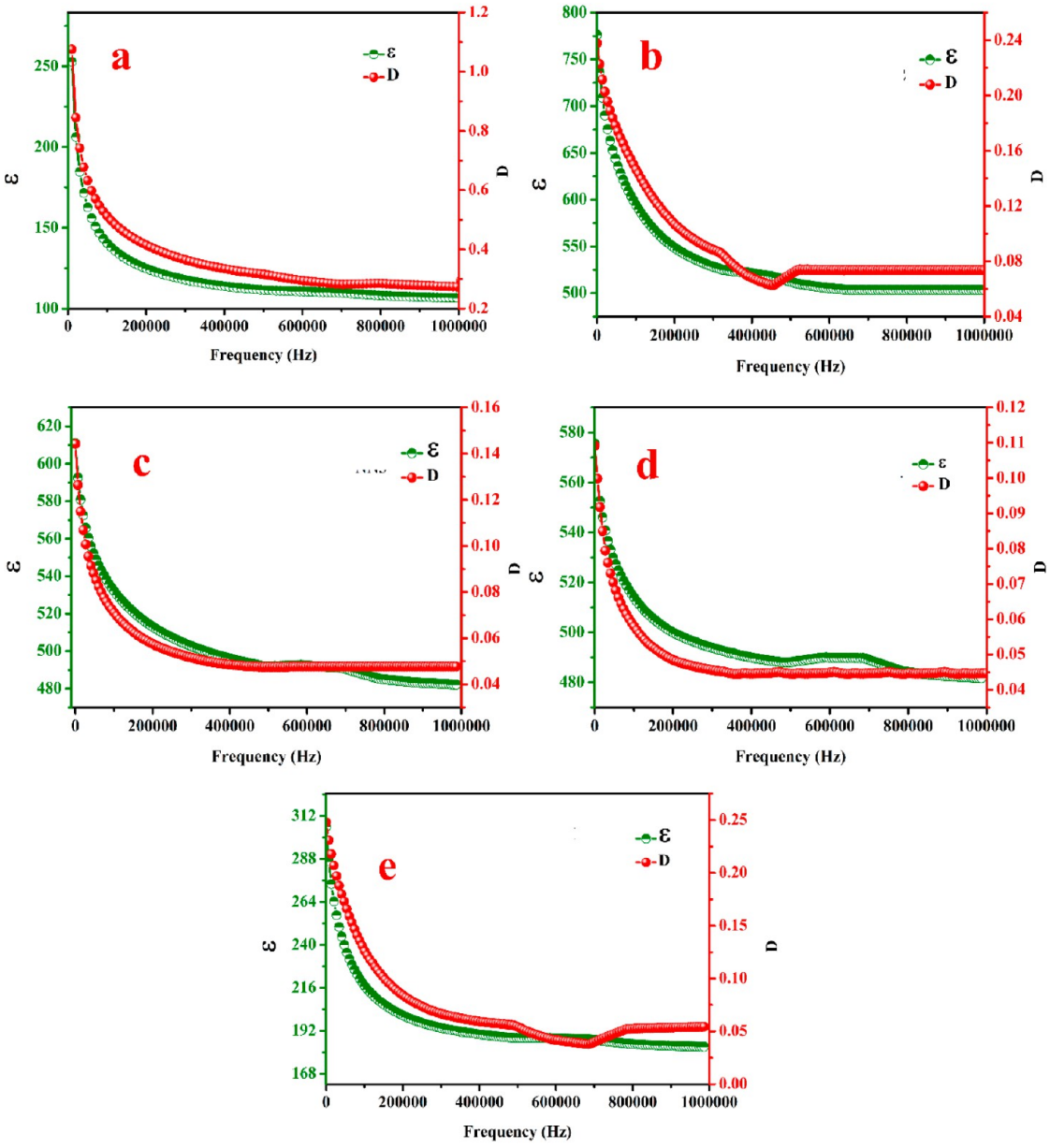

Figure 10. Variation of dielectric constant and dielectric loss with frequency of (a) NN, (b) NN1, (c) NN2, (d) NN3, and (e) NN4 samples at 100 °C.

Figure S7 represents the effect of different scavengers on photocatalytic activity of as-synthesized photocatalysts. Using the results obtained from the quenching experiments, the following possible mechanism for photocatalytic activity was deduced.

$$(\mathrm{NN, NN1{-}NN4}) + h\nu \rightarrow (\mathrm{NN, NN1{-}NN4})(e^{-}_{CB}...h^{+}_{VB})$$

$$(\mathrm{NN, NN1{-}NN4})(e_{CB}^{-}) + O_2 \rightarrow (\mathrm{NN, NN1{-}NN4})O^{-\bullet}$$

$$2O^{-\bullet} + H_2O \rightarrow HO_2^{\bullet} + OH^{-}$$

$$HO_2^{\bullet} + H_2O \rightarrow HO^{\bullet} + H_2O_2$$

$$H_2O_2 \rightarrow 2OH^{\bullet}$$

$$2OH^{\bullet} + \mathrm{MB} \rightarrow CO_2 + H_2O$$

$$(\mathrm{NN, NN1{-}NN4})(h_{VB}^{+}) + \mathrm{MB} \rightarrow \text{degraded product}$$

where NN corresponds to pure $NaNbO_3$ and NN1−NN4 corresponds to 5−20 mol % Ta-doped $NaNbO_3$, respectively. The electrons in the conduction band after photoexcitation are represented by e_{CB}^{-}, and the holes in the valence band are designated by h_{VB}^{+}.

3.8.2. Photocatalytic Water Splitting Studies. The photocatalytic activity for hydrogen generation using water splitting phenomenon was evaluated for all the samples. The evolution of hydrogen was measured as a function of time for pure $NaNbO_3$ and NN1−NN4 compositions. Herein, we have reported the H_2 evolution for pure sample and NN2 sample with the highest activity and for NN4 to show with a further increase in Ta concentration photocatalytic activity decreases. Figure 9a shows the rates of H_2 generation of pure $NaNbO_3$, 10 mol % Ta-doped $NaNbO_3$ (NN2), and 20 mol % Ta-doped $NaNbO_3$ (NN4) samples under full arc irradiation. During the investigation, it

https://doi.org/10.1021/acsomega.1c07250
ACS Omega 2022, 7, 16952−16967

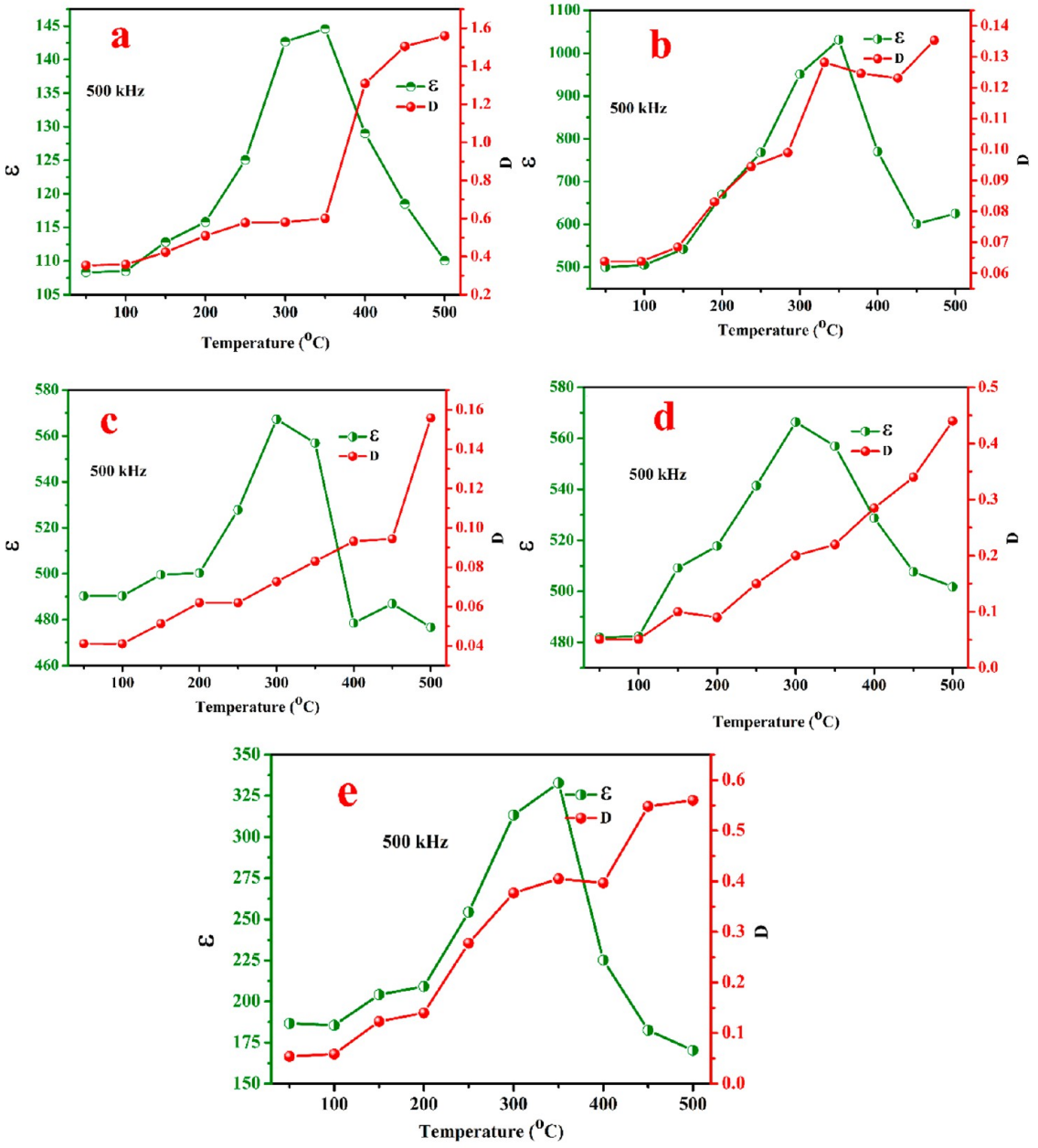

Figure 11. Variation of dielectric constant and dielectric loss with temperature of (a) NN, (b) NN1, (c) NN2, (d) NN3, and (e) NN4 samples at 500 kHz.

was observed that the amount of H_2 generated was equal to 1.7, 21.4, and 5.5 mmol g^{-1} in the presence of pure $NaNbO_3$, NN2, and NN4 respectively, in 8 h. From the obtained results the highest H_2 production rate was observed in the NN2 sample. With the increasing concentration of Ta, the photocatalytic H_2 evolution activity increases until 10 mol % as sample NN2 shows the highest activity. Thus, the improvement in photocatalytic activity could be attributed to the increase in surface area and change in the reduction potential of the conduction band. With addition of Ta at the Nb sites, the position of the conduction band is altered and is shifted to a more negative reduction potential, which favors the easy separation of photogenerated charge carriers, while as with a further increase in Ta concentration, photocatalytic activity decreases, which is attributed to an increase in band gap due to which photo-absorption activity of a material is reduced.

To further investigate the reason responsible for enhanced photocatalytic activity of as synthesized Ta-doped $NaNbO_3$ nanostructures, photoluminescence (PL) investigation was carried out. Figure 9b represents the PL spectra of the synthesized pure $NaNbO_3$ and different mole % Ta-doped $NaNbO_3$ samples. From the PL spectra, the excitation peak for all the samples was observed at 472 nm. It was also observed that with an increase in Ta doping, the intensity of the peak present at 472 nm decreases, thus confirming the delay in the recombination of photogenerated charge carriers due to the entrapment of excitons.[48]

3.9. Dielectric Studies. Variation of dielectric properties including dielectric constant (ε) and dielectric loss (D) of all the synthesized samples was evaluated with frequency ranging from 20 Hz to 1 MHz at 100 °C. Also, the variation of (ε) and (D) of pristine $NaNbO_3$ and Ta-doped $NaNbO_3$ nanoparticles with a

https://doi.org/10.1021/acsomega.1c07250
ACS Omega 2022, 7, 16952−16967

temperature range (50−500 °C) was measured at 500 kHz. Figure 10a−e shows the variation of (ε) and (D) of pure $NaNbO_3$ and 5, 10, 15, and 20 mol % Ta doped $NaNbO_3$ nanoparticles with frequency at 100 °C. From Figure 10, it was observed that with an increase in frequency, the dielectric constant of as-prepared nanoparticles decreases rapidly at lower frequencies and remains stable and constant at higher frequencies. At lower frequencies, all these nanoparticles show high dielectric dispersion. Similar behavior is demonstrated by dielectric loss, which shows high value at lower frequency and decreases with an increase in frequency. The whole dielectric behavior can be explained based on Maxwell−Wagner interfacial polarization theory of dielectrics.[49,50] At lower frequencies, different structures including space charge, dipoles, and ions contribute to the overall polarization of the materials. At lower frequencies, these structures have enough time to undergo the relaxation process and follow the external applied electric field. With an increase in frequency, the space charge polarization does not get enough time to follow the applied electric field and therefore is relaxed out at higher frequencies. According to Koop's theory, another important reason for the decrease in the dielectric constant with frequency is contribution from grain boundaries and grains which are relaxed out at higher frequencies.[51] The energy dissipation or dielectric loss of all the synthesized samples decreases with increase in frequency because of the contribution of dipoles toward polarization. The variation of the dielectric loss curve follows similar behavior as that of the dielectric constant. The high value to dielectric loss at lower frequency is due to high resistive grain boundaries which are more prominent than grains.

In addition, the variation of (ε) and (D) in pure $NaNbO_3$ and Ta-doped $NaNbO_3$ with temperature is shown in Figure 11a−e. The detailed measurements of dielectric properties were carried out in the temperature range of 50−500 °C at a selected frequency of 500 kHz with a temperature interval of 50 °C. From Figure 11, it was observed that at 500 kHz all the samples show an increase in the dielectric constant with an increase in temperature. In the pure $NaNbO_3$ sample, the dielectric constant increases in the temperature range 50−400 °C and shows a maximum value at 400 °C. With a further increase in temperature, the dielectric constant decreases. The temperature having a maximum value of the dielectric constant corresponds to a Curie temperature of the sample.[52] From dielectric dependence on temperature, at 500 kHz dielectric constant, maxima were observed in all the samples with different compositions. From the results, it was observed that with an increase in the dopant concentration, the dielectric constant maximum is shifted toward lower temperature. Also, with an increase in the doping concentration, the dielectric constant increases up to 5 mol % doping of Ta in $NaNbO_3$, and with a further increase in dopant concentration, the dielectric constant starts decreasing.

The increase in dielectric constant as compared to pure $NaNbO_3$ up to 5 mol % Ta doping is attributed to the change in the microstructure of the samples. It had been observed that dielectric properties of the material are influenced by grain size, porosity, applied temperature, and substituent/dopant concentration. As investigated by SEM analysis, the concentration of Ta as dopant in $NaNbO_3$ plays an important role in controlling the microstructure. As reported earlier, it is observed that grain size distribution plays an important role in the dielectric properties of the material. The variation of the dielectric constant in Ga doped $K_{1-x}Na_xNbO_3$ and $BaTiO_3$ with grain size was reported, and from these results it was explained how domain twining, microstructure, and internal stress at the grain boundaries play an important role in the dielectric constant of the material.[53] In this report, we speculate similar behavior responsible for the variation of the dielectric constant with temperature. As observed from dielectric analysis, the sample having 5 mol % Ta doping concentration has the highest value of the dielectric constant and it decreases with a further increase of Ta doping. This behavior is attributed to electronic or ionic defect migration taking place on addition of a dopant in the host material.[53]

All the synthesized samples with different concentration ranges have comparable dielectric loss all over the measuring temperature range as shown in Figure 11. The increase in dielectric loss with temperature of as-prepared samples is attributed to the change in mobility of ionic defects with an increase in temperature. Table 3 represents the value of the dielectric constant and dielectric loss at 100 °C and 500 kHz frequency of as-prepared samples.

Table 3. Dielectric Constant and Dielectric Loss Values of As-Prepared Samples at 500 kHz and 100 °C

sample	dielectric constant	dielectric loss
NN	111	0.031
NN1	510	0.06
NN2	491	0.044
NN3	488	0.047
NN4	188	0.05

3.10. AC Conductivity Studies. To understand the conduction mechanism and evaluate the parameters controlling the process of conduction for pure and Ta-doped $NaNbO_3$ nanoparticles, AC conductivity measurements were carried in the frequency range 20 Hz to 1 MHz at 50 °C as shown in Figure S8. From conductivity measurements, it was observed that with an increase in frequency, the conductivities of all the samples increase. The presence of hopping channels is responsible for hopping conduction; therefore, with an increase in frequency, the hopping channels are facilitated and becomes more active, which promotes more charge carrier hopping. The Jonscher power law (eq 4) was used to understand the underlying mechanism for the conduction behavior of as-prepared nanoparticles.

$$\sigma = A\omega^{\eta} \tag{4}$$

where A is a constant, ω represents angular frequency, and exponent n represents the frequency dependent slope. The value of n determines the mechanism responsible for the conduction behavior of the samples. For $\eta < 1$ and $\eta > 1$ conduction follows the Maxwell−Wagner type mechanism and barrier hopping conduction mechanism, respectively. From fitting of the conductivity plots of different samples, it was observed that all the samples have $\eta < 1$ and follow the conduction hopping barrier mechanism, which involves short-range translational hopping along with the small and large polaron hopping mechanisms. From AC conductivity measurements, it was also observed that conductivity first decreases with an increase in Ta %, and with a further increase in Ta above 5 mol %, conductivity increases.

https://doi.org/10.1021/acsomega.1c07250
ACS Omega 2022, 7, 16952−16967

4. CONCLUSION

Successful synthesis of pristine $NaNbO_3$ and Ta-doped $NaNbO_3$ nanohierarchal building blocks was carried out by a simple hydrothermal route. XRD and electron microscopic investigations confirm the formation of highly crystalline, monophasic, typical single layered nanoflakes of pristine $NaNbO_3$, and with an increase in percentage doping of Ta, thin layered nanosheet formation was restricted. The addition of Ta in $NaNbO_3$ owned a strong influence on its band structure, which obviously improves the photocatalytic activity and dielectric properties of $NaNbO_3$. The highest photocatalytic water splitting activity (21 μmol/g) and 89% removal of MB organic dye was observed in 10 mol % Ta-doped $NaNbO_3$ as compared to pure $NaNbO_3$. Similarly, in 5 mol % Ta-doped $NaNbO_3$, an enhanced dielectric constant of 510 was observed. Improved photocatalytic activity and a dielectric constant of Ta-doped $NaNbO_3$ was attributed to the improvement in the separation of photogenerated charge carriers, absorption ability, and structural changes due to Ta doping.

■ ASSOCIATED CONTENT

Supporting Information

The Supporting Information is available free of charge at https://pubs.acs.org/doi/10.1021/acsomega.1c07250.

Figure S1, detailed view of hierarchitectures of NN, NN1, NN2, NN3, and NN4 samples and magnified micrographs of NN, NN1, NN2, NN3, and NN4 nanohierarchitectures; Figure S2, EDAX spectral analysis of as prepared samples; Table S1, atomic percentage and stoichiometry of as-synthesized samples obtained by using EDAX analysis; Figure S3 and S4, UV−visible DRS spectra, Kubelka−Munk plot of synthesized samples, and UV−visible spectra of dye solution in the presence of light and synthesized photocatalysts; Figure S5, LC-MS spectra of MB dye after photocatalysis; Figure S6, degradation fragments formed from MB dye after the photocatalytic degradation process; section S1, mechanism of the photocatalytic dye degradation process deduced by using different scavengers; Figure S7, variation of photocatalytic activity in the presence of different scavengers; and Figure S8, variation of conduction with frequency for as-synthesized samples at 100 °C (PDF)

■ AUTHOR INFORMATION

Corresponding Author

Tokeer Ahmad − *Nanochemistry Laboratory, Department of Chemistry, Jamia Millia Islamia, New Delhi 110025, India;* orcid.org/0000-0002-7807-315X; Phone: 91-11-26981717; Email: tahmad3@jmi.ac.in

Authors

Umar Farooq − *Nanochemistry Laboratory, Department of Chemistry, Jamia Millia Islamia, New Delhi 110025, India;* orcid.org/0000-0001-8068-7962

Jahangeer Ahmed − *Department of Chemistry, College of Science, King Saud University, Riyadh 11451, Saudi Arabia;* orcid.org/0000-0003-2331-6406

Saad M. Alshehri − *Department of Chemistry, College of Science, King Saud University, Riyadh 11451, Saudi Arabia*

Yuanbing Mao − *Department of Chemistry, Illinois Institute of Technology, Chicago, Illinois 60616, United States;* orcid.org/0000-0003-2665-6676

Complete contact information is available at: https://pubs.acs.org/10.1021/acsomega.1c07250

Notes

The authors declare no competing financial interest.

■ ACKNOWLEDGMENTS

T.A. thanks the SPARC scheme (Grant SPARC/2018-2019/P843/SL) of Ministry of Education, Govt. of India for financial support. U.F. especially thanks UGC, New Delhi for the Research Fellowship. The authors also acknowledge the measurement support provided through the DST PURSE program at CIF, Jamia Millia Islamia, and AIIMS, New Delhi, for electron microscopic studies. Y.M. would like to thank the support by the IIT start-up funds. The authors extend their sincere appreciation to Researchers Supporting Project Number (Grant RSP-2021/29), King Saud University, Riyadh, Saudi Arabia.

■ REFERENCES

(1) Gust, D.; Moore, T. A.; Moore, A. L. Mimicking photosynthetic solar energy transduction. *Acc. Chem. Res.* **2001**, *34*, 40−48.

(2) Li, P.; Ouyang, S.; Xi, G.; Kako, T.; Ye, J. The effects of crystal structure and electronic structure on photocatalytic H_2 evolution and CO_2 reduction over two phases of perovskite-structured $NaNbO_3$. *J. Phys. Chem. C* **2012**, *116*, 7621−7628.

(3) Alshehri, S. M.; Ahmed, J.; Ahamad, T.; Alhokbany, N.; Arunachalam, P.; Al-Mayouf, A. M.; Ahmad, T. Synthesis, characterization, multifunctional electrochemical (OGR/ORR/SCs) and photodegradable activities of $ZnWO_4$ nanobricks. *J. Sol-Gel Sci. Technol.* **2018**, *87*, 137−146.

(4) Shi, H.; Chen, G.; Zhang, C.; Zou, Z. Polymeric g-C_3N_4 coupled with $NaNbO_3$ nanowires toward enhanced photocatalytic reduction of CO_2 into renewable fuel. *ACS Catal.* **2014**, *4*, 3637−3643.

(5) Ahmad, T.; Farooq, U.; Phul, R. Fabrication and photocatalytic applications of perovskite materials with special emphasis on alkali-metal-based niobates and tantalates. *Ind. Eng. Chem. Res.* **2018**, *57*, 18−41.

(6) Gu, Q.; Zhu, K.; Zhang, N.; Sun, Q.; Liu, P.; Liu, J.; Wang, J.; Li, Z. Modified solvothermal strategy for straightforward synthesis of cubic $NaNbO_3$ nanowires with enhanced photocatalytic H_2 evolution. *J. Phys. Chem. C* **2015**, *119*, 25956−25964.

(7) Tong, H.; Ouyang, S.; Bi, Y.; Umezawa, N.; Oshikiri, M.; Ye, J. Nano-photocatalytic materials: possibilities and challenges. *Adv. Mater.* **2012**, *24*, 229−251.

(8) Farooq, U.; Phul, R.; Alshehri, S. M.; Ahmed, J.; Ahmad, T. Electrocatalytic and enhanced photocatalytic applications of sodium niobate nanoparticles developed by citrate precursor route. *Sci. Rep.* **2019**, *9*, 4488.

(9) Mehtab, A.; Ahmed, J.; Alshehri, S. M.; Mao, Y.; Ahmad, T. Rare earth doped metal oxide nanoparticles for photocatalysis: A perspective. *Nanotechnology* **2022**, *33* (1−31), 142001.

(10) Fujishima, A.; Honda, K. Electrochemical photolysis of water at a semiconductor electrode. *Nature* **1972**, *238*, 37−38.

(11) Farooq, U.; Ahmed, J.; Alshehri, S. M.; Ahmad, T. High-surface-area sodium tantalate nanoparticles with enhanced photocatalytic and electrical properties prepared through polymeric citrate precursor route. *ACS Omega* **2019**, *4*, 19408−19419.

(12) Farooq, U.; Chaudhary, P.; Ingole, P. P.; Kalam, A.; Ahmad, T. Development of cuboidal $KNbO_3$@α-Fe_2O_3 hybrid nanostructures for improved photocatalytic and photoelectrocatalytic applications. *ACS Omega* **2020**, *5*, 20491−20505.

(13) Ahmad, T.; Phul, R.; Khan, H. Iron oxide nanoparticles: An efficient nano-catalyst. *Curr. Org. Chem.* **2019**, *23* (9), 994−1004.

(14) Mohan, S.; Mao, Y. Molten salt synthesized submicron perovskite $La_{1-x}Sr_xCoO_3$ particles as efficient electrocatalyst for water electrolysis. *Front. Mater.* **2020**, *7*, 117−126.

(15) Abraham, A.; Gupta, S. K.; Mohan, S.; Abdou, H.; Mao, Y. Defect induced optical and electrochemical properties of $Pr_2Sn_2O_7$ nanoparticles enhanced by Bi^{3+} doping. *J. Mater. Res.* **2020**, *35* (9), 1214−1224.
(16) Mortazavi-Derazkola, S.; Zinatloo-Ajabshir, S.; Salavati-Niasari, M. Novel simple solvent-less preparation, characterization and degradation of the cationic dye over holmium oxide ceramic nanostructures. *Ceram. Int.* **2015**, *41* (8), 9593−9601.
(17) Ahmed, J.; Ahamad, T.; Alhokbany, V.; Almaswari, B. M.; Ahmad, T.; Hussain, A.; Al-Farraj, E. S. S.; Alshehri, S. M. Molten salts derived copper tungstate nanoparticles as bifunctional electro-catalysts for electrolysis of water and supercapacitor applications. *ChemElectroChem.* **2018**, *5*, 3938−3945.
(18) Naaz, F.; Farooq, U.; Khan, M. A. M.; Ahmad, T. Multifunctional efficacy of environmentally benign silver nanospheres for organic transformation, photocatalysis and water remediation. *ACS Omega* **2020**, *5* (40), 26063−26076.
(19) Phul, R.; Khan, M. A. M.; Sardar, M.; Ahmed, J.; Ahmad, T. Multifunctional electrochemical properties of synthesized non-precious iron oxide nanostructures. *Crystals* **2020**, *10* (1−14), 751.
(20) Jain, S. K.; Fazil, M.; Naaz, F.; Pandit, N. A.; Ahmed, J.; Alshehri, S. M.; Mao, Y.; Ahmad, T. Silver doped SnO_2 nanostructures for photocatalytic water splitting and catalytic nitrophenol reduction. *New J. Chem.* **2022**, *46*, 2846−2857.
(21) Ahmed, J.; Alam, M.; Majeed Khan, M.A.; Alshehri, S. M. Bifunctional electro-catalytic performances of $NiMoO_4$-NRs@RGO nanocomposites for oxygen evolution and oxygen reduction reactions. *J. King Saud Univ. Sci.* **2021**, *33*, 101317.
(22) Kato, H.; Asakura, K.; Kudo, A. Highly efficient water splitting into H_2 and O_2 over lanthanum-doped $NaTaO_3$ photocatalysts with high crystallinity and surface nanostructure. *J. Am. Chem. Soc.* **2003**, *125*, 3082−3089.
(23) Bajorowicz, B.; Reszczyńska, J.; Lisowski, W.; Klimczuk, T.; Winiarski, M.; Słoma, M.; Zaleska-Medynska, A. Perovskite-type $KTaO_3$−reduced graphene oxide hybrid with improved visible light photocatalytic activity. *RSC Adv.* **2015**, *5*, 91315−91325.
(24) Wang, X.; Chen, G.; Zhou, C.; Yu, Y.; Wang, G. N-doped Nb_2O_5 sensitized by carbon nitride polymer−synthesis and high photocatalytic activity under visible light. *Eur. J. Inorg. Chem.* **2012**, *2012* (11), 1742−1749.
(25) Kumar, S.; Khanchandani, S.; Thirumal, M.; Ganguli, A. K. Achieving enhanced visible-light-driven photocatalysis using type-II $NaNbO_3$/CdS core/shell heterostructures. *ACS Appl. Mater. Interfaces* **2014**, *6*, 13221−13233.
(26) Farooq, U.; Naz, F.; Phul, R.; Pandit, N. A.; Jain, S. K.; Ahmad, T. Development of heterostructured ferroelectric $SrZrO_3$/CdS photocatalysts with enhanced surface area and photocatalytic activity. *J. Nanosci. Nanotechnol.* **2020**, *20*, 3770−3779.
(27) Modak, B.; Modak, P.; Ghosh, S. K. Improving visible light photocatalytic activity of $NaNbO_3$: a DFT based investigation. *RSC Adv.* **2016**, *6*, 90188−90196.
(28) Jana, P.; Mata Montero, C.; Pizarro, P.; Coronado, J.M.; Serrano, D.P.; de la Pena O'Shea, V.A. Photocatalytic hydrogen production in the water/methanol system using Pt/RE:$NaTaO_3$ (RE = Y, La, Ce, Yb) catalysts. *Int. J. Hydrog. Energy* **2014**, *39*, 5283−5290.
(29) Torres-Pardo, A.; Jiménez, R.; García-González, E.; González-Calbet, J. M. Phase coexistence in $NaNb_{(1-x)}Ta_xO_3$ materials with enhanced dielectric properties. *J. Mater. Chem.* **2012**, *22*, 14938−14943.
(30) Yadav, A.; Fahad, M.; Satapathy, S.; Sarun, P. M. Effect of tantalum on the temperature dependent electrical characteristics of $NaNb_{1-x}Ta_xO_3$ ($0.0 < x < 0.3$) ceramics between 400−560 °C. *J. Alloys Compd.* **2019**, *797*, 902−911.
(31) Fan, M.; Hu, B.; Yan, X.; Song, C.; Chen, T.; Feng, Y.; Shi, W. Excellent visible-light-driven photocatalytic performance of Cu_2O sensitized $NaNbO_3$ heterostructures. *New J. Chem.* **2015**, *39*, 6171−6177.
(32) Khatoon, S.; Ahmad, T. Synthesis, optical and magnetic properties of Ni-doped ZnO nanoparticles. *J. Mater. Sci. Eng. B* **2012**, *2* (6), 325−333.
(33) Ahmad, T.; Ganguly, A.; Ahmed, J.; Ganguli, A. K.; Al-Hartomy, O. A. Nanorods of transition metal oxalates: A versatile route to the oxide nanoparticles. *Arab. J. Chem.* **2011**, *4*, 125−134.
(34) Ahmad, T.; Ganguli, A. K. Synthesis of nanometer-sized particles of barium orthotitanate prepared through a modified reverse micellar route: structural characterization, phase stability and dielectric properties. *J. Mater. Res.* **2004**, *19* (10), 2905−2912.
(35) Salavati-Niasari, M.; Ghanbari, D.; Davar, F. Synthesis of different morphologies of bismuth sulfide nanostructures via hydrothermal process in the presence of thioglycolic acid. *J. Alloys Compd.* **2009**, *488*, 442−447.
(36) Ghanbari, D.; Salavati-Niasari, M.; Sabet, M. Preparation of flower-like magnesium hydroxide nanostructure and its influence on the thermal stability of poly vinyl acetate and poly vinyl alcohol. *Compos. B. Eng.* **2013**, *45*, 550−555.
(37) Salavati-Niasari, M.; Davar, F.; Loghman-Estarki, M. R. Controllable synthesis of thioglycolic acid capped ZnS (Pn) 0.5 nanotubes via simple aqueous solution route at low temperatures and conversion to wurtzite ZnS nanorods via thermal decompose of precursor. *J. Alloys Compd.* **2010**, *494*, 199−204.
(38) Zinatloo-Ajabshir, S.; Morassaei, M. S.; Amiri, O.; Salavati-Niasari, M. Green synthesis of dysprosium stannate nanoparticles using Ficus carica extract as photocatalyst for the degradation of organic pollutants under visible irradiation. *Ceram. Int.* **2020**, *46*, 6095−6107.
(39) Zhu, L. P.; Bing, N. C.; Wang, L. L.; Jin, H. Y.; Liao, G. H.; Wang, L. J. Self-assembled 3D porous flowerlike α-Fe_2O_3 hierarchical nanostructures: synthesis, growth mechanism, and their application in photocatalysis. *Dalton Trans.* **2012**, *41*, 2959−2965.
(40) Kruczek, M.; Talik, E.; Kania, A. Electronic structure of $AgNbO_3$ and $NaNbO_3$ studied by X-ray photoelectron spectroscopy. *Solid State Commun.* **2006**, *137*, 469−473.
(41) Deng, Q.; Li, M.; Wang, J.; Zhang, P.; Jiang, K.; Zhang, J.; Hu, Z.; Chu, J. Exploring optoelectronic properties and mechanisms of layered ferroelectric $K_4Nb_6O_{17}$ nanocrystalline films and nanolaminas. *Sci. Rep.* **2017**, *7*, 1883.
(42) Katsumata, K.; Cordonier, C. E. J.; Shichi, T.; Fujishima, A. Photocatalytic activity of $NaNbO_3$ thin films. *J. Am. Chem. Soc.* **2009**, *131*, 3856−3857.
(43) An, L.; Onishi, H. Electron−hole recombination controlled by metal doping sites in $NaTaO_3$ photocatalysts. *ACS Catal.* **2015**, *5*, 3196−3206.
(44) Liu, Q.; Zhang, Q.; Zhang, L.; Dai, W.-L. Highly efficient single-crystalline $NaNb_{1-X}Ta_XO_3$ (x = 0.125) wires: The synergistic effect of tantalum-doping and morphology onphotocatalytic hydrogen evolution. *J. Mater. Sci. Technol.* **2020**, *54*, 20−30.
(45) Thommes, M.; Kaneko, K.; Neimark, A. V.; Olivier, J. P.; Rodriguez-Reinoso, F.; Rouquerol, J.; Sing, K. S. W. Physisorption of gases, with special reference to the evaluation of surface area and pore size distribution (IUPAC Technical Report). *Pure Appl. Chem.* **2015**, *87*, 1051−1069.
(46) Kumar, S.; Yadav, N.; Kumar, P.; Ganguli, A. K. Design and comparative studies of Z-Scheme and type II based heterostructures of $NaNbO_3$/$CuInS_2$/In_2S_3 for efficient photoelectrochemical applications. *Inorg. Chem.* **2018**, *57*, 15112−15122.
(47) Phul, R.; Shrivastava, V.; Farooq, U.; Sardar, M.; Kalam, A.; Al-Sehemi, A. G.; Ahmad, T. One pot synthesis and surface modification of mesoporous iron oxide nanoparticles. *Nano-Struct. Nano-Objects* **2019**, *19* (1−6), 100343.
(48) Singh Vig, A.; Rani, N.; Gupta, A.; Pandey, O.P. Influence of Ca-doped $NaNbO_3$ and its heterojunction with g-C_3N_4 on the photoredox performance. *Sol. Energy* **2019**, *185*, 469−479.
(49) Xu, J.; Feng, B.; Wang, Y.; Qi, Y.; Niu, J.; Chen, M. BiOCl decorated $NaNbO_3$ nanocubes: A novel p-n heterojunction photocatalyst with improved activity for ofloxacin degradation. *Front. Chem.* **2018**, *6*, 393−402.

https://doi.org/10.1021/acsomega.1c07250
ACS Omega 2022, 7, 16952−16967

(50) Ahmad, T.; Ubaidullah, M.; Lone, I. H.; Kumar, D.; Al-Hartomy, O. A. Microemulsion synthesis, structural characterization and dielectric properties of $Ba_{1-x}Pb_xZrO_3$ ($0.05 \leq x \leq 0.20$) nanoparticles. *Mater. Res. Bull.* **2017**, *89*, 185−192.
(51) Koops, C. G. On the dispersion of resistivity and dielectric constant of some semiconductors at audiofrequencies. *Phys. Rev.* **1951**, *83*, 121−124.
(52) Kwon, D.; Goh, Y.; Son, D.; Kim, B.; Bae, H.; Perini, S.; Lanagan, M. Temperature-and frequency-dependent dielectric properties of sol−gel-derived $BaTiO_3$-$NaNbO_3$ solid solutions. *J. Electron. Mater.* **2016**, *45*, 631−638.
(53) Atamanik, E.; Thangadurai, V. Dielectric properties of Ga-doped $Na_{0.5}K_{0.5}NbO_3$. *J. Phys. Chem. C* **2009**, *113*, 4648−4653.

https://doi.org/10.1021/acsomega.1c07250
ACS Omega 2022, 7, 16952−16967